Imaging-based Dispersion in CT Coreflooding Experiments

Ali Fadili[1,*], and *Steffen* Berg[2,]

[1]Shell Kuwait Exploration and Production B.V., 20th Floor, Sahab Tower, Salhiya, Kuwait
[2]Shell Global Solutions International B.V., Grasweg 31, 1031HW Amsterdam, The Netherlands

Abstract. Monitoring core flooding experiments with medical CT scanners has become increasingly accessible since the introduction of medical CT scanners in the geosciences in the mid-1980s. While initially 3D imaging was mainly used to assess rock heterogeneity in a qualitative manner, over the past decades the technique has matured to acquiring time series of 3D images ("4D") in-situ during core flooding experiments. The medical CT scanners commonly used for this purpose (but also other 3D imaging methods) have a finite scanning time even for very coarse spatial resolution. Depending on the injection rate, this scanning time may not be negligible compared to advection time of fluids in the core. As it occurs in photography of moving objects where a long shutter time leads a "motion blurring", such effect also occurs in core flooding experiment because of the relative movement of the fluids and the imaging system. This "image dispersion" can then be mis-interpreted as physical (hydrodynamic) dispersion or leads to incorrect heterogeneity characterization. To demonstrate the impact, we consider the scenario of solute transport. For illustration purpose we start with a homogeneous case described with a 1D dispersive model. We show that the degree of image-dispersion on the concentration profiles comes as an additional smearing of the profiles as the relative velocity of the CT imaging to the fluid front increases. We then proceed with 3D heterogeneous case where it is demonstrated how imaging-based dispersion leads to the misinterpretation of flow in spatially resolved heterogeneity as hydrodynamic dispersion. The findings suggest that the imaging-based dispersion effect needs to be considered for practically all 4D imaging methods such as CT, PET, MRI of dynamic processes with respect to the interpretation of heterogeneity and its effects, e.g. hydrodynamic dispersion, capillary dispersion of a flow front.

1 Introduction

Non-destructive investigation techniques such as X-ray computed tomography (CT), nuclear magnetic resonance imaging (MRI), positron emission tomography (PET) are increasingly used to determine concentration profiles and saturation distributions in core flooding experiments [1-8]. They are used to assess rock heterogeneity, determine the dispersion coefficient/dispersivity or compute relative permeability. Examples include imaging of tracer tests in heterogeneous rock, recovery processes such as enhanced oil recovery, trapping in underground storage of CO_2 and hydrogen, , and providing in-situ saturation profiles for determining relative permeability and capillary pressure. For studying flow and transport phenomena, 4D imaging is realized through time sequences of 3D images. The acquisition of 3D images is, however, not instantaneous but requires a finite acquisition time. When imaging core flooding experiments, during that finite imaging time Δt, the fluid front propagates (mainly in the flow direction) along the core which leads to a motion artefact. In **Fig. 1** we illustrate the case of imaging tracer experiments by using a synthetically generated solute concentration spatial profiles which mimics the situation of an experiment conducted in a relatively homogeneous core and modelled using a 1D advection-dispersion equation (ADE) [9,10]. As the scanner catches up with the front, the concentration it sees will be higher than the actual value as indicated by the blue arrows. The difference in the reported concentrations gets higher as the front advances in the core.

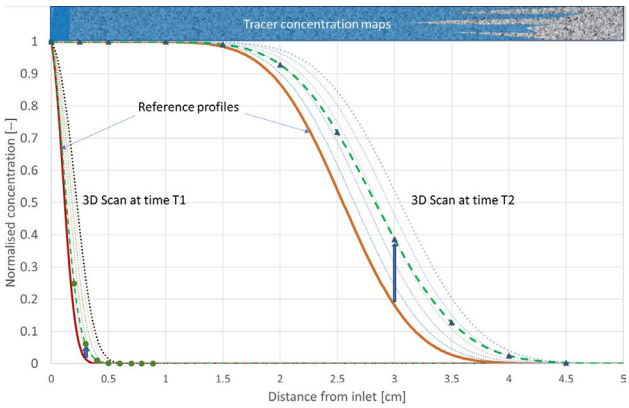

Fig. 1. Illustration of the image dispersion for a homogeneous core modelled using 1D ADE. The plot shows the hypothetical positions of a moving front at $0.1 \times v_s$ at early and late times. The dotted lines are profiles each with 6s lag time. The dashed green lines represent fits of the concentration values seen by

*Corresponding author: Ali.Fadili@shell.com

the scanner (dot and triangle symbols) with an ADE, showing increased *imaged* dispersion compared with the ground truth solid lines.

For instance, in CT scanning transmission images are obtained from 360 degrees viewing angles. MRI and PET require also significant acquisition time [7, 8], ranging from 30s for medical CT scanners to several minutes in MRI, depending on whether the acquisition is in 1D, 2D or 3D.

In essence, the advancement of a flow front cannot be captured by instantaneous snapshots which leads to well-known signal smearing [11,12]. For a given flow rate, the impact of this smearing effect could be reduced by faster imaging. But that would – because of limitations in imaging technology - typically lead to poorer signal-to-noise levels on the individual 3D snapshots and overall, not improve the fidelity of the 4D images.

The primary objective of this work is to raise awareness of some of the limitation of the 4D imaging, and to assess the impact of this motion blurring, which we will refer to as "imaging-based dispersion" since blurred profiles have a dispersion-like character. One would intuitively expect that imaging 10-times faster than the flow velocity would be sufficient to have negligible impact of blurring, but we will show that this is not the case.

We demonstrate the effect by selecting tracer dispersion (solute transport) as an example. We show how for imaging speeds up to 10x faster than the flow velocity the effect of imaging-based dispersion can be quantified by an advection-dispersion equation (ADE). However, for faster flows this parameterization breaks down. Hence this finite imaging-based artefact needs to be assessed for each experiment to an acceptable level. We demonstrate how imaging-based dispersion can mask heterogeneity, which could then lead to misinterpretation as hydrodynamic dispersion. Lastly, we offer for specific scenarios concepts for improving image acquisition protocols that can help suppressing the imaging-based dispersion effects.

2 Imaging dispersion in solute transport

To illustrate the effect of imaging-based dispersion, we consider the situation of solute transport of a passive tracer through a porous domain at Darcy scale.

2.1 Homogeneous case - 1D view

The starting point is the 1D modelling of a tracer experiment in a homogeneous porous domain with a synthetic data set for which the ground truth is known. At the inlet of a porous domain a tracer solution of concentration c_0 [kg/m^3] is injected. The concentration $c(x,t)$ [kg/m^3] at position x and time t is then described by the advection-dispersion equation (ADE), for which the analytical solution can be put in the form:

$$c(x,t) = \frac{c_0}{2}\left[erf\left(\frac{x-vt}{\sqrt{4D_l t}}\right) + exp\left(\frac{xv}{D_l}\right) erf\left(\frac{x+vt}{\sqrt{4D_l t}}\right)\right] \quad (1)$$

where erf is the error function, exp is the exponential function, v is the average frontal speed, and D_l the longitudinal dispersion coefficient [m^2/s] which (assuming negligeable molecular diffusion) can be expressed as

$$D_l = \alpha_l \cdot v \quad (2)$$

with the dispersivity α_l [m]. The extent of imaging-based dispersion is dependent on location and imaging speed relative to flow velocity. **Fig. 1** shows 2 profiles at different locations, close to inlet or more advanced within the core, and the expected impact on the profiles seen by the imaging system at those two different locations. To isolate the effects of velocity alone, we fixed the location of the reference profile and varied the ratio of the frontal velocity v to the scanner linear velocity v_s. The latter is simply the length of the imaged core L (here 5 cm) divided by the imaging time Δt

$$v_s = L/\Delta t \quad (3)$$

For a medical CT scanner, a typical imaging time is $\Delta t = 30\ s$ [13]. **Fig. 2** illustrates this case with the concentration profiles generated using eq. (1) for two different velocity ratios.

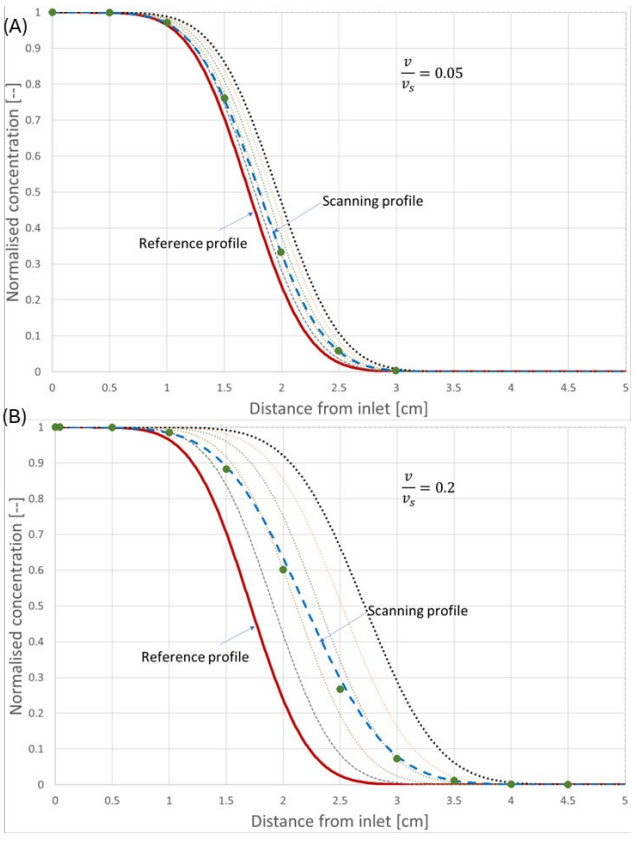

Fig. 2. Synthetically created tracer dispersion curves demonstrating the impact of finite imaging time on the effective tracer dispersion for a case with a low injection rate (A) and a high injection rate (B) in relation to the scan speed v_s. The red solid lines are the "ground truth" from eq. (1) at the same injected PV when the scan starts at the inlet of the core. The solid triangles and dots are the concentrations that the CT scanner "sees" because of its finite imaging time. They are constructed via concentration profiles with increments of 6s lag time (thin dotted lines). Dashed blue lines represent a fit of the symbols with eq. 1.

In **Fig. 2** the dotted lines are 6s lagged profiles starting from the reference profile. The dots are concentration values seen by the scanner as it sweeps the core from the inlet to the outlet. They are fitted with eq. (1), but now with an effective velocity v_e and an effective dispersivity α_e. As shown in **Fig. 2**, the image-dispersed profiles (dashed-lines) is clearly velocity dependent.

To quantify the effect of increased relative front speed to the linear scanner velocity, we generated a succession of profiles as per **Fig. 2** and plotted the fitting parameters v_e and α_e against the velocity ratio v/v_s, as shown in **Fig. 3**. The left vertical axis shows the ratio of the dispersitivities α_e/α_l while the right vertical axis is for the ratio of the effective velocity to the frontal velocity, v_e/v. As the front velocity v increases, the effective dispersivity α_e increases significantly. This shows clearly that the dispersion derived from the scanner data overestimates the hydrodynamic dispersion – depending on v/v_s – by factors. As the scanner catches up with the front, the front has some time to disperse even further increasing the concentration at the location where it gets recorded by the scanner. Also, because of the finite time needed to complete the full 3D scan, the front advances during that time, leading to an effective velocity v_e higher than the ground-truth front velocity v.

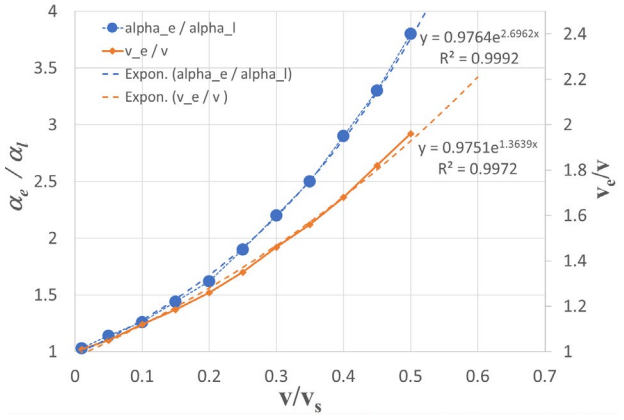

Fig. 3. Impact of imaging-based dispersion as a function of flow velocity v over imaging speed v_s, v/v_s. Left vertical axis: effective dispersivity α_e normalized to the ground-truth longitudinal dispersivity α_l. Right vertical axis: effective velocity v_e normalized to the frontal velocity v. α_e and v_e are obtained as per the fits in **Fig. 2** with eq. (1) for ratio v/v_s from 0,001 to 0.5.

Fig. 3 shows that for imaging 10x faster than flowing, i.e., $v/v_s \approx 0.1$, we already see a significant increase in the fitted dispersivity α_e, about 25% higher than the "real" hydrodynamic dispersivity α_l. Similarly, the effective velocity is about 10% higher than the frontal velocity. Hence, even for a completely homogeneous medium, imaging 10x faster than the front velocity is not sufficient. For this particular case, increasing the imaging speed by a factor of 10 to $v/v_s \approx 0.01$ might reduce the impact of imaging-based dispersion to less than 5%, which might be acceptable in relation to uncertainties of concentration/saturation measurements which is typically ~5% for medical CT. This means completing a full 3D scan within a factor 100 faster than the front velocity.

The range of flow over imaging velocities v/v_s depicted in **Fig. 3** covers the range of experiments conducted in the literature. Without going into details, many medical CT imaged single and multi-phase flow core floods conducted at reservoir-representative flow rates of 1 ft/day [15] fall in the range of $0.001 \leq v/v_s \leq 0.01$ for which the impact of imaging-based dispersion is negligible. There are, however, also several experiments with $0.01 \leq v/v_s \leq 0.1$ where an over-estimation of properties derived from frontal profiles of up to 30% can be expected. There are also a few experiments conducted for $v/v_s > 0.1$ where the impact is likely more significant. Note that these estimations assume homogeneous core plugs.

The situation portrayed via this synthetically generated example is not hypothetical but reflects the current experimental reality. **Fig. 3** can serve as a guide to assess the uncertainty of parameters associated with the frontal shape of concentration or saturation profiles such as dispersion coefficient/dispersivity, capillary dispersion/capillary pressure and relative permeability of flow experiments with imaging. It can also be instrumental to design flow experiments with imaging and optimize the acquisition protocol.

As **Fig. 3** shows, the imaging-based dispersion does not only affect the dispersivity α_e but also the effective velocity v_e, simply because during the finite imaging the front also moves forward, i.e., has advanced its position, which makes the effective speed v_e appear faster than v.

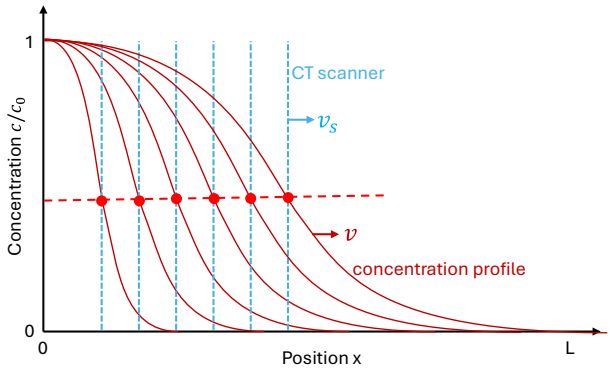

Fig. 4. Situation where the flow velocity approaches the imaging velocity, $v = v_s$. The CT scans (vertical dashed blue lines)

follow the concentration profile with equal velocity and therefore intersect always at the same constant concentration. Therefore, the resulting concentration profile $c(x,t)$ is constant.

Note that for $v/v_s \geq 1$ the effective concentration profile $c(x,t)$ obtained by 4D imaging simply cannot be represented by eq. (1). Once $v > v_s$ the imaging only "see" the injected value, and in the case $v = v_s$ the reported value is also $c(x,t) = const.$, and the constant value will depend on whether the imaging is started before or after the injection. The situation is sketched in **Fig. 4**.

A constant concentration is not represented by eq. (1) anymore. However, from the trends of eq. (1) for increasing D_l the $c(x,t)$ profiles become more elongated and with decreasing slope. In the limit of $D_e \to \infty$ the profile would become flat. That is the reason for the divergence of D_e and α_e for $v \to v_s$. At the same time, the fitting with eq. (1) can no longer localize the position x of the concentration profile. Hence, the trends of α_e and v_e in **Fig. 3** are plausible.

2.2 Heterogeneous case - 3D view

Solute transport with 4D imaging is often conducted for the purpose of mapping the resolved heterogeneity of cores. Traditional methods are based on mapping first the 3D porosity field, e.g. by differential dry-wet imaging, and then assign a 3D permeability field using a porosity-permeability correlation [14]. One complication is that porosity-permeability distributions often show a wide spread, i.e. for the same porosity a wide range (several orders of magnitude) of different permeability is possible, meaning there is a priori no unique solution. This leads to an overall uncertainty in the 3D permeability field of the heterogeneous rock implying that the 3D permeability field needs to be validated. The dispersion of the tracer test is then used to reduce the uncertainty in digital twin model with respect to the permeability field. One approach is to use the tracer experiment in an inverse manner, to validate and iteratively refine the 3D porosity and permeability distribution to build a calibrated Digital twin. There are also more advanced methods where tracer data is directly used to determine 3D permeability fields, such as using the arrival time distribution in combination with a pre-trained machine learning tool to determine the 3D permeability distribution of the core [16].

It is important to make here the distinction between resolved and sub-resolution heterogeneity in the 3D imaging technique. In the context of solute transport, sub-resolution heterogeneity is generally captured via hydrodynamic dispersion on the length scale that is resolved by the imaging method, which is effectively the scale of smoothing of solute concentration fields (fronts). The spatially resolved heterogeneity can be explicitly mapped in 3D and respective properties such as porosity and permeability fields assigned.

The question is now how imaging-based dispersion interferes with resolving the heterogeneity that is within the imaging resolution. From the homogeneous 1D case we have already seen that finite imaging time can lead to a dispersion-like blurring, and we quantified it as an increased effective dispersivity α_e and a higher effective velocity front apparent v_e.

To extend the analysis to the 3D case, we built a 3D digital twin of a core plug from a heterogeneous carbonate rock. A CT scan of the core plug is displayed in **Fig. 5** with 3 scans along the 3 directions, taken in the middle of the core. In the case of a 3D heterogeneous core plug, all the processes described for the homogeneous case before are now distributed through the core via the velocity heterogeneity, leading a more complex image-dispersion process. The derivation of the porosity map is based on a differential imaging of the CT scans of dry core (air saturated) and wet core (brine saturated). This allows a reasonable determination of the porosity map. However, the permeability map remains unknown as it is a flow-based parameter. Following the workflow published in [14] the permeability field is determined by assuming a porosity-permeability correlation. To minimize the number of parameters a power-law relation was used:

$$K(x,y,z) = K_0 \left(\frac{\phi(x,y,z)}{\phi_{av}}\right)^n \quad (4)$$

where ϕ_{av} is the average porosity. The model parameter K_0 is mainly determined by the pressure drop across the core, while the permeability contrast is mainly controlled by the exponent n. The latter is determined by the tracer dispersion. Hence, controlling the image-dispersion becomes key in the heterogeneity characterization.

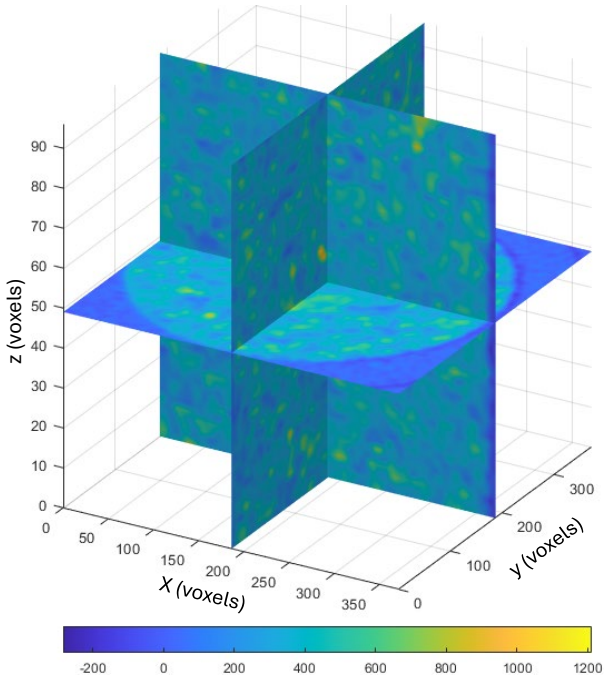

Fig. 5. Hounsfield values of a CT scan of the heterogeneous core plug used to demonstrate the effect of image-dispersion in

3D heterogeneous core. Three orthogonal slices are displayed corresponding to differential imaging (dry/wet) of a core by medical CT. Size of the core is typical of a SCAL experiment (~2inch long and 1.5inch diameter).

The derived 3D porosity map based on differential imaging of CT scans as in **Fig. 5** is shown in **Fig. 6** top.

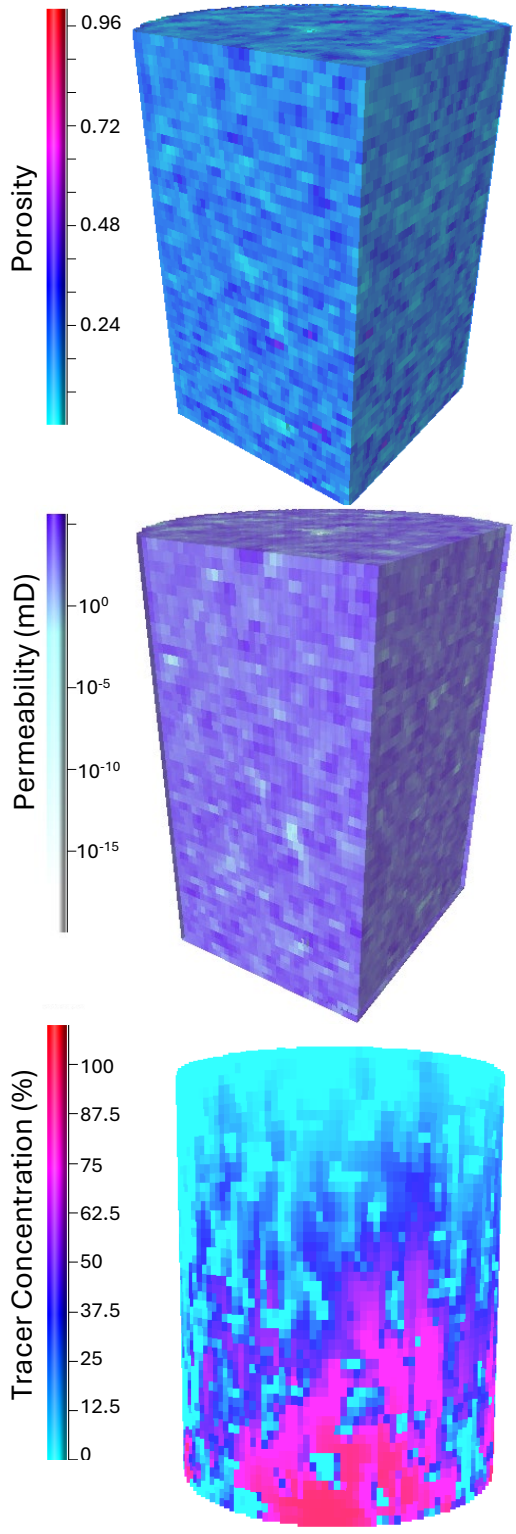

Fig. 6. Top: 3D map of the porosity obtained by differential imaging (dry/wet) of a core from medical CT. Size of the core is typical of a SCAL experiment (~2inch long and 1.5inch diameter). Middle: 3D map of the permeability derived using the power-law correlation eq. (1). Bottom: snapshot of the tracer concentration in the case of 2cm^3/min injection after ~10min injection.

Fig. 6. also shows the corresponding permeability map (based on eq. (4)) and a snapshot of the tracer concentration map for the case of 2 cm^3/min injection after about 10min injection. The numerical simulation of the tracer test was designed to minimize numerical dispersion by using very small grid blocks (~1mm^3) with a small stepping (~0.5min) to ensure high accuracy of the numerical solution. The objective is to capture the complex flow paths induced by the variability in porosity and permeability, while ensuring that the numerical artefacts remain significantly smaller than the heterogeneity effects.

Fig. 7 shows the 3D map of the simulated (single-phase) velocity field for 3 different flow rates: Q_w = 0.1, 1, 2 cm^3/min in line with typical experimental conditions. It also shows the concentration profiles along the middle line (dashed yellow line) of the core at three different times: 0s (red line, "ground truth"), lagged 15s (blue line) and lagged 30s (green line, end of scanning time), assuming the scanner starts the 3D scanning (slice per slice) from the inlet at time 0s. As discussed earlier for the homogeneous case, while the scanner moves towards the outlet, so does the concentration front. When the scanner is halfway through, the concentration value that it sees is on the blue curve (shown by a star for the case of Q = 2cm^3/min). On this line, the error on the concentration is about 20% (higher). While in stagnant regions (light blue, dashed circle) of the core, which are bypassed by flow through higher permeable regions, no image-dispersion occurs, in high velocity regions (red) it can be significant, hence leading a distorted view of the 3D map heterogeneity using the concentration field. As the flow rate increases, we get into the same process as discussed for the homogeneous, whereby the front has already progressed with some measurable value before the imaging system catches up with front.

In addition, as the imposed flow rate increases, the contrast in the local velocities increases as does the effect of the image-dispersion on the signal measured by the imaging system. Because the 3D velocity cannot be known a priori, this local smearing cannot be corrected. As discussed for the homogeneous case, the image-dispersion is exacerbated towards the outlet of the core, and the distortion between the local concentration reported by the imaging and the "ground truth" can be quite significant.

Following the same approach as in the 1D homogeneous case, the concentration profiles are obtained as cross-section average $c(x,t)$. This averaging introduces the typical shape of a concentration profile $c(x)$ subject to hydrodynamic dispersion as per eq. 1 . They are then interpreted by fitting a dispersion model eq. (1).

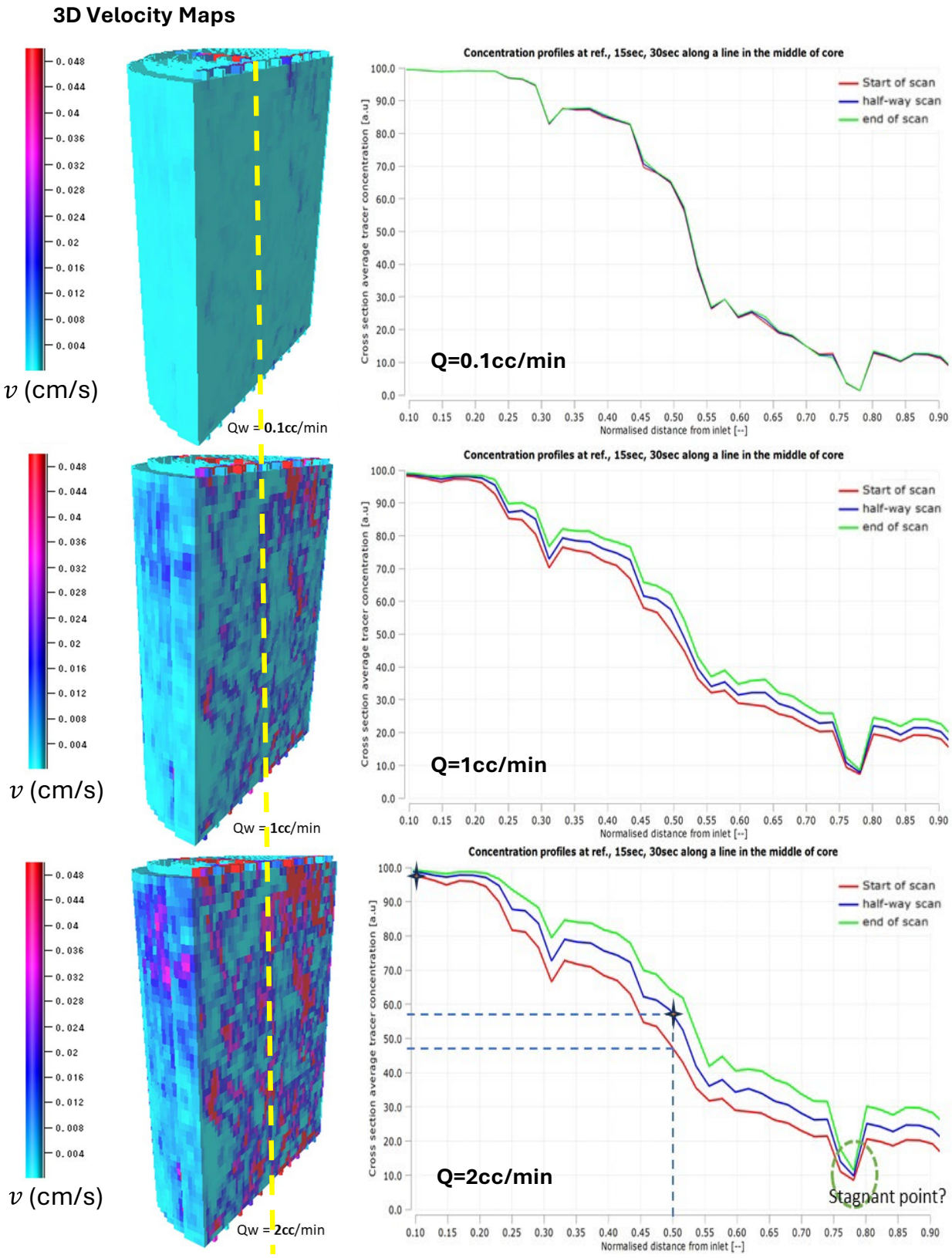

Fig. 7. Right: 3D velocity fields for injection rates of 0.1, 1 and 2 cm^3/min illustrating the complexity of the flow field. Left: concentration profiles at 3 different times: reference, 15s lagged and 30s lagged. This illustrates that the larger variation in local flow velocity the wider range of misinterpretation by imaging-based dispersion.

In the 1D homogeneous case where synthetic data was used, the ground truth α_l was known and the effect of image-dispersion could be easily estimated. For real situations the a-priori dispersion is not known, as in our example of a real heterogeneous carbonate rock, the imaging-based dispersion prevents us from determining the correct value. What is known is an estimate of the resolved heterogeneous permeability field. To estimate the associated image-dispersion, we proceeded as for the 1D case by running a case with explicit hydrodynamic dispersion (α_L, α_T) and an effective flow rate Q_e and by tuning these parameters so that the corresponding concentration profile goes through the two red dots in **Fig. 8** resulting in profile given by the red line with symbols, which is the expected profile to be reported by the imaging system. The result is a smoothed concentration distribution, as shown in **Fig. 8** on the top right, that masks the true distribution of heterogeneity (top left), which would be seen by a solute transport simulation without the hydrodynamic dispersion, reflecting the image that an infinitely fast scanner would take.

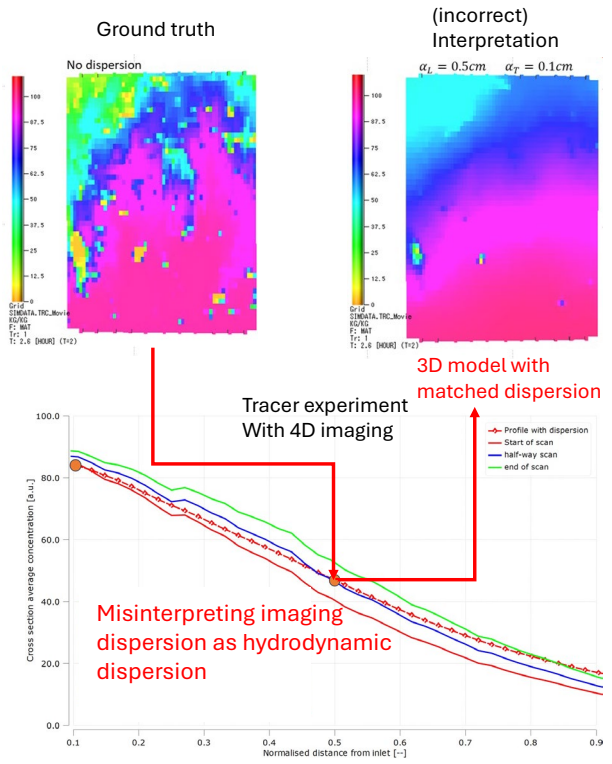

Fig. 8. Cross section average tracer concentration profiles at different scanning time lags: start (red), half-way (blue), end (green) for flow rate 2 cm^3/min. Circles indicate the points "seen" by the scan at the start and half-way. Dashed line with symbols represents the fitting curve, using hydrodynamic dispersion ($\alpha_L = 0.5\ cm, \alpha_T = 0.1\ cm$) with an effective flow rate of 2.15cm^3/min, mimicking the expected profile CT scan, and illustrating the associated image dispersion.

The imaging-based dispersion implies that the local concentration derived from the 4D imaging can be quite different from the real 3D distribution. The image-dispersion adds more blurring to concentration fields that in heterogeneous rocks -because of the complex flow field – is distributed in all directions. This is then incorrectly interpreted as a rock that has less resolved heterogeneity but more hydrodynamic dispersion. In some sense, in the case of 3D heterogeneous rock, the consequence of imaging-based dispersion is a loss in spatial resolution.

Fundamentally, the error introduced by the finite time imaging can be better estimated by considering the ideal case where a snapshot of the full core is taken leading a sequence of slices as:

$$S(z_1, t_0), S(z_2, t_0), \dots, S(z_i, t_0), \dots, S(z_n, t_0) \quad (5)$$

and the actual finite imaging case where the sequence can be described as:

$$S(z_1, t_0), S(z_2, t_1), \dots, S(z_i, t_i), \dots, S(z_n, t_n) \quad (6)$$

where the z_i is the position in the core of the slice being image at time t_i. From these two sequences, it becomes evident that the error:

$$e_i = S(z_i, t_i) - S(z_i, t_0) \approx (t_i - t_0)\frac{\partial S}{\partial t}(z_i, t_0) \quad (7)$$

increases with the finite imaging time as the content of the slice when it is imaged is time dependent. This simple representation also demonstrates that this error cannot fundamentally be eliminated even with the fastest imaging system. Hence the objective of this analysis is to stress on the awareness of this artefact in 4D imaging to avoid complex interpretation, and to help the experiment to be designed within the imaging capabilities range where this error can be manageable. Note also that considering the average front velocity as criterion for imaging can be misleading, as for example, a high permeability streak would generate significant image-dispersion compared to the rest of the core.

3 Imaging dispersion in two-phase flow

While the effect was so far demonstrated for solute transport in single-phase flow, imaging-based dispersion will also affect multi-phase core flooding experiments, where 4D imaging is used to monitor transient dynamic processes. That includes in particular unsteady-state relative permeability experiments, where the shape of the immiscible displacement front which is controlled by the interplay between viscous and capillary forces, contributes to the interpretation of capillary pressure and relative permeability [17,18]. Imaging-based dispersion may impact the shape of the displacement front in similar ways as the concentration front in solute transport shown in **Fig. 2**. That would then lead to a misinterpretation, resulting in an over-estimation of capillary pressure or smaller relative permeability. Similar consequences may occur when directly interpreting saturation profiles $S_w(x,t)$ and compute time derivatives $\partial S_w/\partial t$ and spatial derivatives $\partial S_w/\partial x$, capillary dispersion coefficient

$D_c(S_w)$ to invert the $S_w(x,t)$ data directly to relative permeability and capillary pressure using fractional flow theory [19]. For relatively homogeneous core and relatively low flow rate (~1 foot/day) a CT imaging time of 30s leads to $v/v_s \approx 10^{-3}$ [17] may be acceptable as according to **Fig. 3** it should exhibit a negligible degree of imaging-based dispersion. However, low flow rate may exacerbate the capillary control of the flow, which might lead to unwanted effects. Hence, the balance between viscous and capillary forces now needs also to integrate the effects of potential image-dispersion artefact for each experimental situation.

In 3D two-phase flow the effects of imaging-based dispersion may become more complex in similar ways as the 3D solute concentration profiles. The 3D saturation maps might not be consistent anymore with capillary pressure dynamic and relative permeability. The local saturation $S_w(x,t)$ is controlled by the interplay between the local viscous and capillary forces controlled by porosity-permeability heterogeneity and fluid properties [20] which generate local capillary end-effects [21]. That is exploited in inverse modelling approaches [22] to determine the spatial distribution of permeability and capillary pressure to determine relative permeability in the viscous limit and in the capillary limit. These results may become affected by imaging-based dispersion when interpreting unsteady-state experiments [23].

4 Optimizing the Imaging Protocol

The above discussion highlighted some of the sources of measurement and interpretation artefact for the transport of a tracer. For multi-phase flows, these artefacts can even worsen because of additional flow effects (e.g. capillary pressure jumps). While the imaging remains a very powerful tool to get insights into the flow process in a non-destructive approach, a different approach/protocol to obtain reliable data for a quantitative interpretation is required. Supported with numerical simulation of the flow process, the objective becomes to get artefact free experimental data which can be used to constrain sufficiently the numerical model to align it with the experiment for its validation. Hence, 4D imaging may not be required and instead accurate effluent curves could suffice to constraint 3D flow models. **Fig. 9** shows a schematic of an imaging system aimed at measuring effluent curves at two distinct locations on the core plug. The simpler mechanics involved in this system are expected to allow a significantly shorter scanning time than the time required for generating 3D scans, and the duration of the scanning (with some fixed frequency) is also expected to be longer to be able to generate full accurate effluent curves.

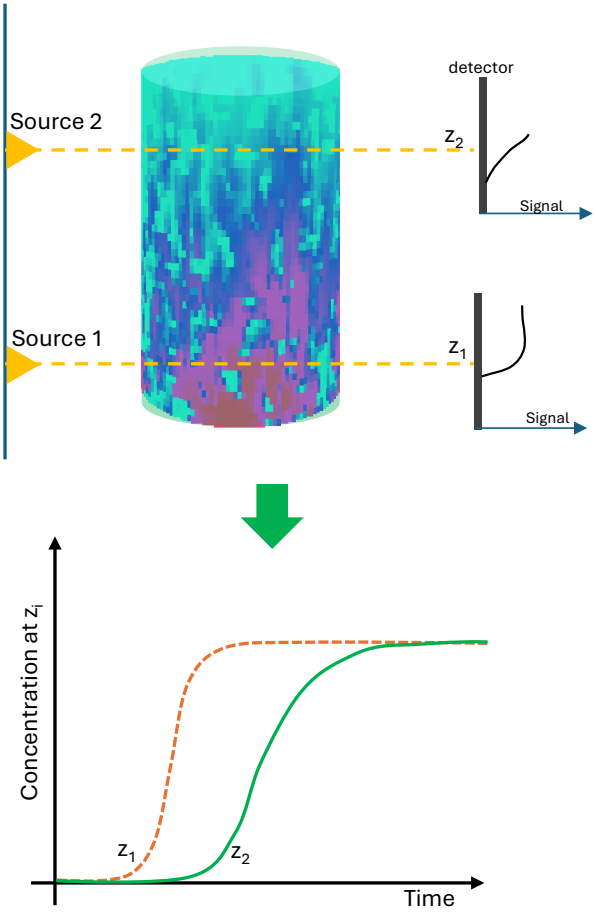

Fig. 10. Schematic of an imaging system aimed at generating accurate effluent curves using two fixed scanning locations. The scanning time for a slice is significantly shorter than for a 3D scan. The mechanics are also simpler hence allowing for longer scanning time to generate effluent curves.

5 Summary & Conclusions

When conducting core flooding experiments with 4D imaging, i.e. capturing time sequences of 3D images, the finite imaging time of CT scanners or of other imaging methods such as MRI and PET causes imaging-based dispersion. This effect needs to be considered when interpreting fluid flow experiments. The reason is that the blurring of fluid fronts can be misinterpreted as increased hydrodynamic dispersion. This would then, for example, affect the estimate of the dispersivity of the rock. The underlying reason of imaging-based dispersion is that during the finite imaging time the fluid fronts move further. What is somewhat surprising is that in homogeneous rocks where concentration and displacement fronts are largely in a 1D setting, the systematic and conceptual evaluation herein shows that imaging 10 times faster than the flow velocity is likely not sufficient. The imaging-based dispersion effects reduce

and minimize indicatively with multiple orders of magnitude (2 at least) faster imaging than flow velocity.

In the more realistic 3D scenarios, the imaging-based dispersion leads to more significant misinterpretation of how heterogeneity impacts flow and solute transport, i.e. heterogeneity which is still spatially resolved at the spatial resolution of the CT scanner can be blurred to the extent where it is interpreted as hydrodynamic dispersion. Because of the heterogeneous imaging dispersion, the 3D interpretation of the concentration/saturation can lead to erroneous interpretation not only of the distribution of the primary variables, but also on any quantity which may depends on them, e.g., saturation and capillary pressure.

The main objective of this study is to raise awareness and provide a relatively simple reference scale in 1D to assess whether the imaging time in relation to flow velocity is such that the results of the experiment remain largely unaffected. But it also offers other options for the imaging. The main point is that dynamic imaging may not always require imaging in 3D. Imaging at two fixed positions can be realized much faster and still captures sufficient information about the fluid dynamic to validate a 3D heterogeneity model.

References

1. S. Akin and A. R. Kovscek. Geological Society, London, Special Publications 215.1 (Jan. 2003), pp. 23–38.
2. M Withjack, C Devier, and G Michael. SPE Western Regional/AAPG Pacific Section Joint Meeting, Long Beach, California, May 2003.
3. J. J. Funk, E. M. Withjack, S. Siddiqui, Sultan M. Al-Enezi, and S. Caliskan. International Symposium of the Society of Core Analysts held in Austin, Texas, USA 18-21 September 2011.
4. H.J. Vinegar. Journal of Petroleum Technology 38.03 (Mar. 1986), pp. 257–259.
5. T. Pak, N. Lopes Archilha, S. Berg, and I. B. Butler. Tomography of Materials and Structures 3 (Sept. 2023), p. 100017
6. S. Van Offenwert, V. Cnudde, and T. Bultreys. Water Resources Research 55.11 (Nov. 2019), pp. 9279–9291.
7. M. S. Zamiri et al. 37th annual Society of Core Analysts international symposium, Fredericton, New Brunswick, 8/25-30/2024.
8. C. Zahasky, T. Kurotori, R. Pini, and S. M. Benson. Advances in Water Resources 127 (May 2019), pp. 39–52.
9. M. Fourar et al. International Symposium of the Society of Core Analysts held in Toronto, Canada, 21-25 August 2005.
10. A. Skauge, B. Vik, S. Pourmohammadi, and K. Spildo. International Symposium of the Society of Core Analysts held in Trondheim, Norway 12-16 September 2006.
11. M. Potmesil and I. Chakravarty. SIGGRAPH Comput. Graph. 17.3 (July 1983), pp. 389–399.
12. J. Cant, W. Jan Palenstijn, G. Behiels, and J. Sijbers. Medical Physics 42.5 (2015), pp. 2709–2717.
13. S. Berg et al., Physics of Fluids 22(11), 113102, 2010.
14. C. Taberner, A. Fadili, S. Berg, F. Marcelis, Y. Gao, R. Bouwmeester, W. De Boever, M. Boone, J. Dewanckele, T. Sorop, J. van der Horst, Image – Third International Meeting for Applied Geoscience & Energy, 28 Aug – 1 Sept 2023, Houston, TX, USA.
15. A. W. Cense, S. Berg, International Symposium of the Society of Core Analysts held in Noordwijk an Zee, Netherlands, 27-30 September 2009, paper SCA 2009-13.
16. Z. Huang, T. Kurotori, R. Pini, S. M. Benson, C. Zahasky, Water Resources Research 58, e2021WR031554, 2022.
17. S. Berg, S. Oedia, H. Ott, International Journal of Greenhouse Gas Control 12, 478-492, 2013.
18. S. Berg, H. Dijk, E. Unsal, R. Hofmann, B. Zhao, V. Ahuja, Computers and Geotechnics 168, 106091, 2024.
19. M. S. Zamiri, N. Ansaribaranghar, F. Marica, A. Ramirez Aguilera, D. Green, C. Caubit, B. Nicot, B. J. Balcom, International Symposium of the Society of Core Analysts held in Fredericton, New Brunswick, Canada, 26-30 August 2024, SCA 2024-1032.
20. A. Fadili, R. Ababou, Water Resources Research 40, W01513, 2004.
21. D. D. Huang, M.M. Honarpour, J. Petrol. Sci. Eng. 19, 103–117, 1998.
22. S. An, N. Wenck, S. Manoorkar, S. Berg, C. Taberner, R. Pini, S. Krevor, Water Resources Research 59, e2023WR035526, 2023.
23. A. Dell'Oca, A. Manzoni, M. Siena, N.G. Bona, L. Moghadasi, M. Miarelli, D. Renna, A. Guadagnini, International Journal of Heat and Mass Transfer 202, 123716, 2023.